Journal of Nuclear Materials 254 (1998) 249–265

Analytical electron microscopy study of surface layers formed on the French SON68 nuclear waste glass during vapor hydration at 200°C

W.L. Gong [a,*], L.M. Wang [a,1], R.C. Ewing [a,1], E. Vernaz [b], J.K. Bates [c], W.L. Ebert [c]

[a] *Department of Earth and Planetary Sciences, University of New Mexico, Albuquerque, NM 87131, USA*
[b] *CEA-VALRHO, B.P. 171, 30205 Bagnols-sur-Ceze Cedex, France*
[c] *Chemical Technology Division, Argonne National Laboratory, Argonne, IL 60439, USA*

Received 18 April 1997; accepted 11 November 1997

Abstract

Extensive solid-state characterization (AEM/SEM/HRTEM) was completed on six SON68 (inactive R7T7) waste glasses which were altered in the presence of saturated water vapor (200°C) for 22, 91, 241, 908, 1000, 1013, and 1021 days. The samples were examined by AEM in cross-section (lattice-fringe imaging, micro-diffraction, and quantitative thin-film EDS analysis). The glass monoliths were invariably covered by a thin altered rind, and the surface layer thickness increased with increasing time of reaction, ranging from 0.5 to 30 μm in thickness. Six distinctive zones, based on phase chemistry and microstructure, were distinguished within the well-developed surface layers. Numerous crystalline phases such as analcime, gyrolite, tobermorite, apatite, and weeksite were identified on the surfaces of the reacted glasses as precipitates. The majority of the surface layer volume was composed of two basic structures that are morphologically and chemically distinct: The A-domain consisted of well-crystallized fibrous smectite aggregates; and the B-domain consisted of poorly-crystallized regions containing smectite, possibly montmorillonite, crystallites and a ZrO_2-rich amorphous silica matrix. The retention of the rare-earth elements, Mo, and Zr mostly occurred within the B-domain; while transition metal elements, such as Zn, Cr, Ni, Mn, and Fe, were retained in the A-domain. The element partitioning among A-domains and B-domains and recrystallization of the earlier-formed B-domains into the A-domain smectites were the basic processes which have controlled the chemical and structural evolution of the surface layer. The mechanism of surface layer formation during vapor hydration are discussed based on these cross-sectional AEM results. © 1998 Elsevier Science B.V.

1. Introduction

The SON68 (SON-68-18-17 LIC2A2Z) inactive 'R7T7' composition is the French reference glass for the light water reactor (LWR) nuclear waste [1]. When in contact with an aqueous solution and/or humid air environment, a high-level nuclear waste (HLW) glass is subjected to chemical attack that results in progressive alteration of the glass matrix. Constituent elements of the glass dissolve into solution, elements initially in the solution diffuse into or are absorbed onto the solid and new phases may appear. These processes lead to the formation of surface layers on the corroded glass. In this paper, vapor hydration refers to the process of altering the chemical and/or physical characteristics of glass surfaces through exposure to water vapor. In saturated water vapor, the actual reactions occur between glass surfaces and a finite but limited amount of water condensed onto the glass surface. Thus, vapor hydration is an alteration process in aqueous solution at an extremely high solid surface area-to-liquid volume (SA/V) ratio. The objective of this study was to simulate the aqueous corrosion of the SON68 glass over extended periods of time by using vapor hydration tests for which the surface area to solution volume ratio was high. Due to high solute concentrations, this accelerates reaction progress and the formation of a characteristic suite of

---

[*] Corresponding author. Tel.: +1-505 272 7142; fax: +1-505 277 8843; e-mail: wgong@unm.edu.

[1] Present address: Department of Nuclear Engineering and Radiological Sciences, The University of Michigan, Ann Arbor, MI 48109-2104, USA.

PII S0022-3115(97)00349-8

secondary alteration phases. The understanding of glass corrosion and radionuclide release can be enhanced by investigating these secondary phases and the microstructural evolution of the surface layer, as glass corrosion may be influenced by mass transport through surface layers. Radionuclide release can also be influenced by nuclide retention in surface layers [2]. Additionally, vapor hydration may be an important corrosion mechanism of nuclear waste glasses in a hydrologically unsaturated geological repository [3].

The secondary phases formed during glass corrosion cannot currently be predicted. Reaction path programs can predict the thermodynamically most stable phases, but they rarely predict the actual phases observed in the tests. Current modeling is usually performed with a restricted set of known phases in the real system [4]. Therefore, secondary phase identification and the compositional and structural evolution of surface layers over time are critical to geochemical modeling of the long-term corrosion behavior of the French nuclear waste glass [5].

The secondary reaction products formed on experimentally reacted waste glasses are often fragile, poorly crystalline, and occur as ultra-thin coatings which make sample preparation and analysis difficult [5–7]. As a result, there are only a limited number of studies of the microstructural evolution of surface layers [8–12], and most researchers have only been able to speculate on the identification of secondary phases or the reaction mechanisms [13–16]. This study involves the microanalytical characterization of the chemical and textural evolution of the surface layers over extended experimental time frames (over 1000 days). We discuss the thickness dependence of the surface layers on the duration of vapor hydration tests; surface layer zoning; the microstructural and compositional evolution during corrosion; the morphology of the corroded surfaces; and the mechanism of surface layer formation by vapor hydration.

2. Experimental techniques

The chemical composition for the SON68 glass is listed in Table 1. The SON68 glass contains 13 wt% of simulated waste oxides. The specific non-active simulates include, MnO_2 for RuO_2; and TcO_2; CoO for RhO_2; NiO for PdO. Pm_2O_3, Sm_2O_3, Eu_2O_3, and Gd_2O_3 are included in the weight fraction of La_2O_3. ThO_2 was used to simulate NpO_2, PuO_2, AmO_2 and CmO_2.

Table 1
The SON68 glass composition (wt%)

SiO_2	45.48	Li_2O	1.98	Sb_2O_3	0.01
Al_2O_3	4.91	ZnO	2.50	TeO_2	0.23
B_2O_3	14.02	SrO	0.33	Cs_2O	1.42
Na_2O	9.86	Y_2O_3	0.20	BaO	0.60
CaO	4.04	MoO_3	1.70	La_2O_3	0.90
Fe_2O_3	2.91	MnO_2	0.72	Ce_2O_3	0.93
NiO	0.74	CoO	0.12	Pr_2O_3	0.44
Cr_2O_3	0.51	Ag_2O	0.03	Nd_2O_3	1.59
P_2O_5	0.28	CdO	0.03	UO_2	0.52
ZrO_2	2.65	SnO_2	0.02	ThO_2	0.33

The glasses were cut from a monolith as rectangular prisms to produce a surface area of approximately 2 cm^2. Vapor hydration tests were conducted by exposing monolithic samples to water vapor at 200°C in a sealed 304 L stainless steel vessel. The volume of the vessel was 23 ml. Enough deionized water (0.25 ml) was added into the vessel so that the vapor was saturated at 200°C. Corrosion of the glass occurred in the thin film of water that was condensed on the sample. Only 0.05 ml of water could condense on the glass sample without dripping off during the vapor hydration tests. At the end of the test, the vessel was removed from the oven and set in a water bath to condense the water vapor onto the bottom of the vessel. Most of the water that was on the sample during the vapor hydration test evaporated when the vessel bottom was cooled. This resulted in the formation of evaporative salts on the sample surface. The pH values for the recondensed water were near 7 for all the test, indicating that the water did not drip from the sample during the test.

The vapor hydration tests were conducted at 200°C for periods of 14, 22, 56, 91, 241, 908, 1000, 1013, and 1021 days. The corresponding samples are referred to as 14D, 22D, 56D, 91D, 241D, 908D, 1000D, 1013D, and 1021D, respectively. In the present work, 91D, 241D, 908D, 1013D, and 1021D were investigated extensively by using scanning electron microscopy with energy dispersive X-ray spectroscopy (SEM/EDS) and analytical electron microscopy with energy dispersive X-ray spectroscopy (AEM). The 22D sample was studied earlier by Jercinovic et al. [17].

The AEM samples prepared by ultramicrotomy preserved the surface layers and allowed the successful description of compositional and microstructural changes in the surface layers from the outermost surface directly in contact with the water vapor to the reaction front which gradually migrated into the bulk glass. For the AEM analysis, a cross-section of several hundred angstroms in thickness was required, perpendicular to the original sample surface. An ultramicrotomy 'slicing' technique [18–20] was used to obtain thin-sections for AEM observations. In this procedure, small chunks containing the reacted surface layer and usually also a small section of unaltered glass were first broken off from the sample, and each of these chunks was then embedded in epoxy resin to form a block. Finally, thin sections, 50–90 nm in thickness, were microtomed from these blocks and transferred to holey carbon filmed copper grids for AEM observation. Ultramicrotomy was completed using a Reichert–Jung Ultracut-E Microtome. The cross-sectional SEM samples were prepared by resin impregnation and by polishing cross-sections of cuts perpendicular to the original surface.

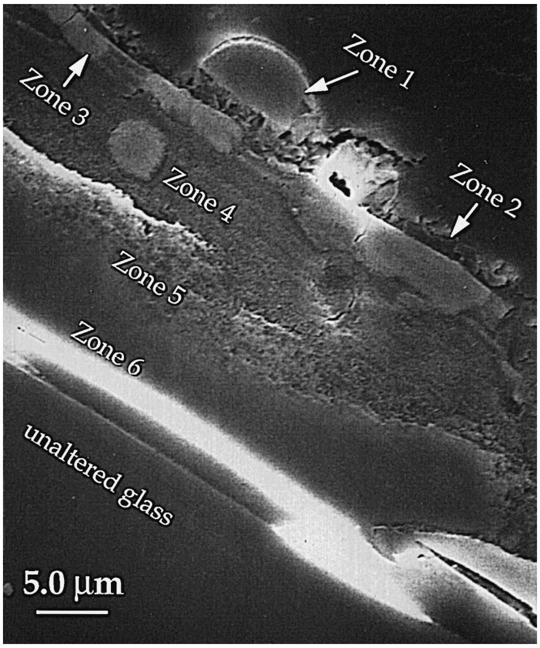

Fig. 1. Cross-sectional SEM micrograph showing a well-developed zones (1–6) on the surface layer (1013D).

Analysis by SEM/EDS was performed on the original reacted surfaces to obtain a large-scale morphological overview, as well as to observe the chemographic relationships of the surface layers. SEM was done using a Hitachi S-800 with a windowless PGT EDS system and a Hitachi S-450. Both were operated at 20 keV.

Analysis by AEM was performed using both a JEM-2000FX electron microscope with an attached Noran TN-5500 EDXS system and a JEM-2010 electron microscope with an attached Oxford Link ISIS EDS system. The microscopes were operated at 200 keV. Extensive TEM imaging included high-resolution transmission electron microscopy (HRTEM), bright-field image (BF), selected area electron diffraction (SAED), and EDS analysis. Most of the chemical compositions reported here were computed using Noran's semi-quantitative software package for metallurgical thin films based on the EDS data acquired by the TN-5500 EDXS system attached to JEM 2000FX. The final compositions were calculated by assuming the stoichiometry of the oxides and were normalized to 100 wt%. The K-factors used for most of the analyzed elements have been well calibrated in the laboratory. The analyzed elements included Na, Al, Si, Fe, Ca, Zn, Ni, Mn, Cr, Mo, Zr, La, Ce, and Nd. The concentrations of Th, U, Cs, Te, Ag, and Co were generally low in the surface layers and their chemical data were only partially reported. Elements such as Li and B which are also important constituents of the original SON68 waste glass, could not be measured using these analytical techniques. Since there was no dripping water during the vapor hydration test, boron is expected to remain in the surface layer. The EDS analyses do not include data for Li, B and water. The accuracy of the EDS analyses was determined to be the ±5% relative error for the major elements and ±20% for the minor elements.

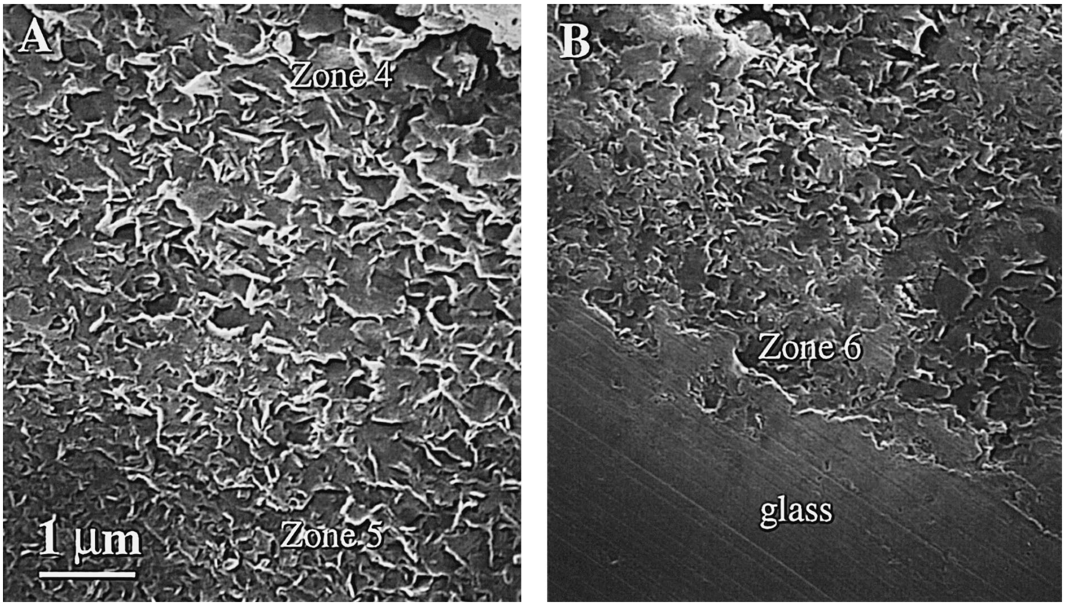

Fig. 2. Enlarged cross-sectional views of Fig. 1 showing the microstructure of Zones 4 and 5 (1013D). Note the higher porosity and larger sizes of individual domains in Zone 4 (A) than in Zone 5 (B). The scale bars for A and B are the same.

3. Results and discussion

3.1. Surface layer zoning

The surface layers were clearly visible by SEM in the backscattered electron images of the cross-sections. Six distinct zones were evident in the most well-developed surface layers (the long-term samples) and could be distinguished based on differences in contrast that are proportional to the backscattered electron density. These zones are nearly parallel to the original glass surface. The zones present a layered appearance and are identified as zones 1–6 in Fig. 1.

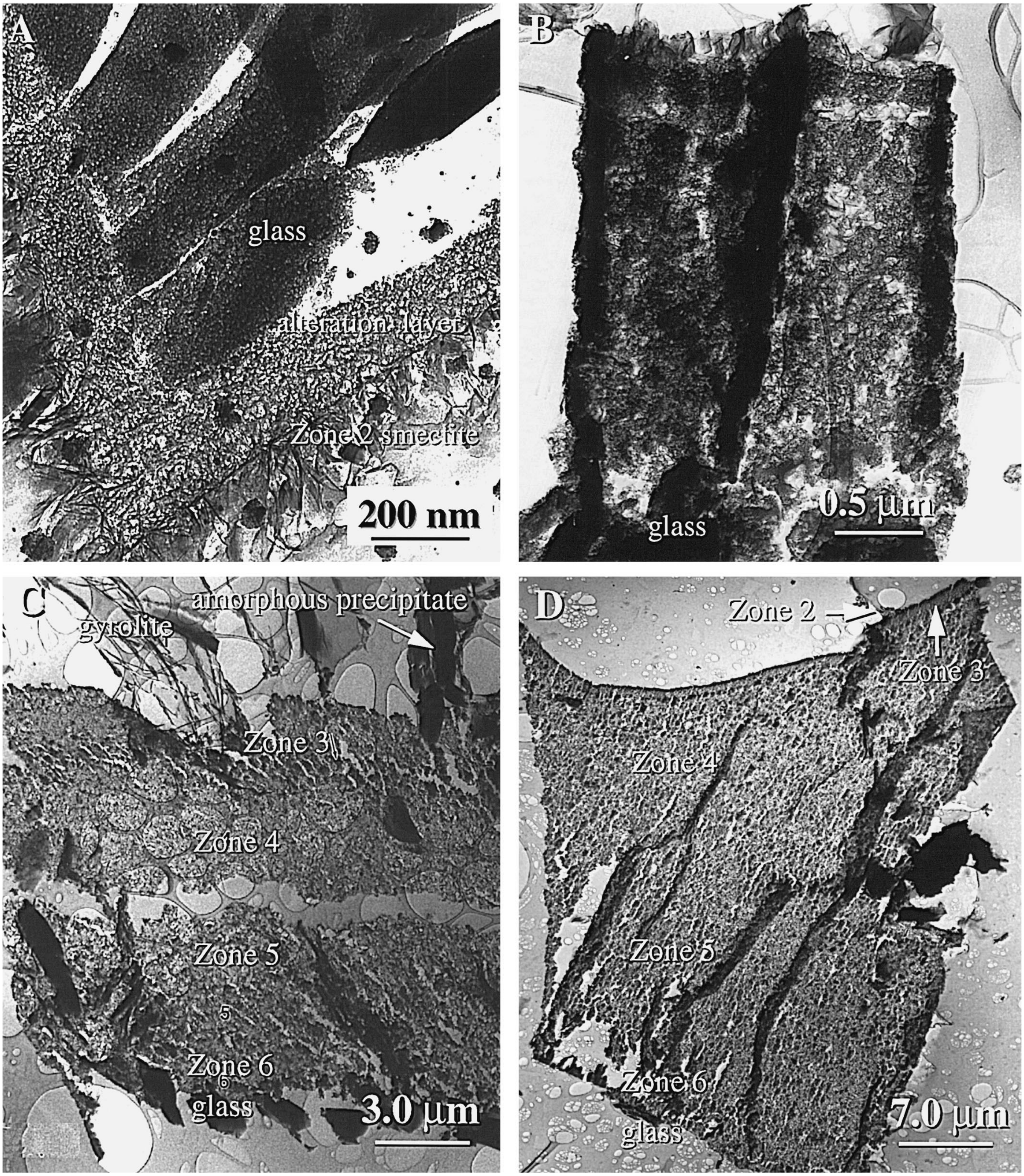

Fig. 3. A sequence of cross-sectional TEM micrographs showing surface layer zoning as a function of time. The circles in the images are the holey carbon substrate. (A) 22D, (B) 241D, (C) 1013D, (D) 1021D.

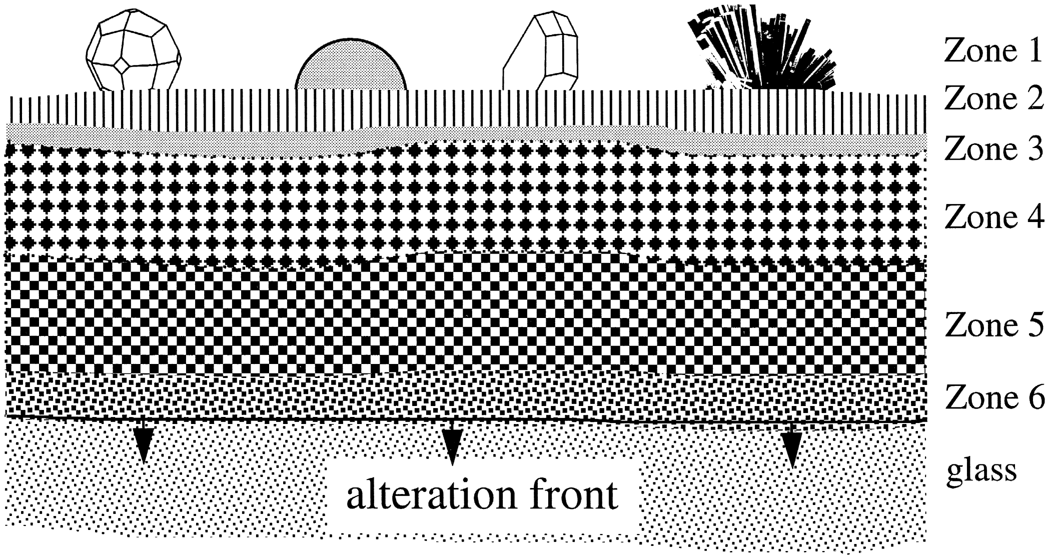

Fig. 4. A schematic illustration of the typical zoning of the surface layers. Zone 1, precipitate zone; Zone 2, vertically oriented fibrous smectite layer; Zone 3, a thin amorphous region high in rare-earth concentrations; Zones 4 and 5 volumetrically comprise the majority of the surface layer and basically consist of A-domains and B-domains; and Zone 6 as nucleation zone.

Zone 1, a precipitation zone, is the outermost layer and is characterized by secondary phases formed by precipitation; Zone 2 is a thin region consisting of well-crystallized and vertically oriented fibrous smectite crystals. This layer has a 'honeycomb' morphology; Zone 3 is a thin, ultrafine-grained region; Zones 4 and 5 account for most of the surface layer volume and mainly consist of finger-like structures and cavities as shown in Fig. 2; Zone 6 is hydrated glass in which smectite crystallites may have nucleated. Fig. 2A, B, which are the enlarged cross-sectional SEM views of Fig. 1, show that the porosity and smectite crystals of Zone 4 are more abundant than in Zone 5. Indeed, the open porosity in the surface layer increases with increasing alteration time.

The zoning of the surface layer is usually less well developed and several inner zones may not be clearly differentiated in the short-term samples, such as 22D and 91D. However, the zoning of surface layers is well developed in the longer-term samples such as 1021D. A sequence of cross-sectional TEM micrographs shows the surface layer zoning as a function of increasing time (Fig. 3).

The surface layer zoning in the SON68 glass is typical of that seen in sample 1021D (Fig. 3D). The surface layer zoning revealed by AEM analysis of an ultramicrotomed sample is consistent with the cross-sectional SEM results. In 1021D, the Zone 1 precipitated layer was not identified because of the heterogeneous distribution of precipitates on the surface, and TEM examination was over a very limited region of the surface layer. Only part of Zone 2 (vertically-oriented smectite layer) was identified. Beneath Zone 2 is the ultrafine-grained mixture of smectite crystallites and amorphous matrices defined by Zone 3. Zones 4 and 5 account for the majority of the volume of the surface layers. Both zones are generally composed of fibrous, coarsely crystalline smectite aggregates and morphologically spherical, less-crystallized, ultrafine-grained domains. Zone 6 is the smectite nucleation zone in the hydrated glassy matrix (0.5–1 μm in thickness). This zone is characterized by the amorphous volumes, cavities and small smectite crystallites. A typical zoning of the surface layer is schematically illustrated by Fig. 4.

The surface layer of 22D only contained two distinct sublayers as shown in Fig. 3A, the outward vertically-grown fibrous smectite layer (here identified as Zone 2) and the inner layer (mostly occupied in volume by Zones 4 and 5). Zone 2 is fibrous, being composed of smectite crystallites with dimensions of 1–20 nm in width and 10–150 nm in length. The interfaces between Zone 2, the inner layer and glass are sharp as shown in Fig. 3A. The inner layer is mostly amorphous with a spherical morphology and some degree of crystallinity, as indicated by a mottled mixture of randomly orientated smectite fibers. The fiber-like smectites are on the order of 1.0 nm or less in width and 10 nm or less in length. The main features of the surface layer of 241D (Fig. 3B) and 1013D (Fig. 3C) lie between those illustrated for 22D (Fig. 3A) and 1021D (Fig. 3D).

After corrosion in saturated water vapor at 200°C, the glass monoliths were invariably covered with a thin alteration rind. We estimated the thickness of the surface layers by cross-sectional SEM examination and by comparison to the cross-sectional AEM results (the precipitation zone was not included in the thickness estimation). The thick-

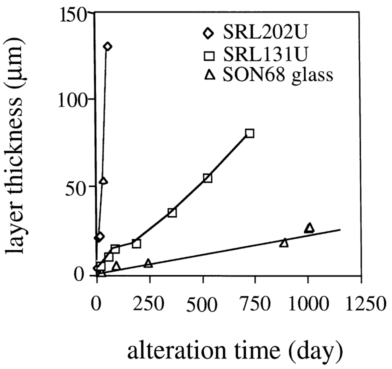

Fig. 5. The thickness of surface layers as a function of alteration time for SON68, SRL131 and SRL 202 glasses. The thickness data for SRL131 (vapor hydration at 150°C) and SRL 202 (vapor hydration at 200°C) glasses were from Refs. [11,12], respectively.

ness of the surface layer increased with the duration of the experiment: 0.5 μm for 22D, 4 μm for 91D; 6 μm for 241D; 16 μm for 908D, 26 μm for 1013D and 30 μm for 1021D.

Fig. 5 shows the evolution of the alteration thickness with increasing time. The mean slope can be used to estimate the order of magnitude of the mean rate of glass alteration under the test conditions. This rate is $\sim 2 \times 10^{-2}$ μm per day. As the glass density is 2.75 g/cm^3, this value corresponds to a mean alteration rate at 200°C under vapor hydration conditions of 5.5×10^{-2} g/m^2d. Surface layer formation is not a constant volume replacement process for the glass. Thus, the derived value represents the upper bound of the mean alteration rate. This value must be compared to the initial rate of glass dissolution (forward rate), which for this glass at 200°C is 102 g/m^2d [21]. This means that the rate of glass alteration under the highly saturated conditions reached under vapor hydration is about 1800 times lower than the forward rate of glass dissolution at this temperature. Other leaching experiments in the pure water at high SA/V give a final rate of glass dissolution under saturation condition at 200°C of 0.5 g/m^2d ($SA/V = 2000\ m^{-1}$) and < 0.4 g/m^2d ($SA/V = 8000\ m^{-1}$) [22].

3.2. Surface morphology and precipitates

A sequence of SEM micrographs shows the morphological evolution of the surfaces during vapor hydration (Fig. 6). 'Honeycomb' smectites usually cover most of the surface. However, in the short-term samples, such as 22D and 91D (Fig. 6A), the smectite layers were less developed on the surfaces as compared to the long-term samples, such as 908D. The abundance of the precipitates on the surfaces increases with increasing time of the vapor hydration test. In 22D, no precipitates were identified on the surface. In 241D, the hydrated silica was a precipitated phase occurring as blocks (Fig. 6B). At higher magnification using a SEM, hydrated silica spheres, ~ 15 nm in size, appear with a rather regular packing, very close to the structure of opal. In the long-term samples, for example 908D (Fig. 6C) and 1013D (Fig. 6D), a great variety and abundance of precipitates appear on the surface.

Precipitates occur frequently on the surfaces of the corroded waste glass. As glass corrodes, it releases elements into the thin film of the condensed water on the glass surface during vapor hydration test. The precipitated phases are either crystalline or amorphous. Based on morphology and EDS/SAED analyses, numerous precipitated secondary phases were identified on the surfaces of the SON 68 glass (Table 2), such as analcime, hydrated Ca-silicate phases, weeksite, apatite, and Na-silicate phases. Analcime precipitates were present on the surface as trapezohedral crystals with voids always filled with apatite rosettes (Fig. 7). Minor precipitates included calcite ($CaCO_3$), gibbsite ($Al(OH)_3$), opal-like silica.

Tobermorite, $Ca_5Si_6O_{16}(OH)_2 \cdot nH_2O$, may be the most frequently occurring hydrated calcium silicate phase precipitated on the surface. The tobermorite structure has infinite $Si_3(O/OH)_9$ chains parallel to the *b*-axis which are linked by calcium atoms coordinated with seven oxygen atoms [24]. This crystal structure accounts for the characteristic fibrous morphology displayed by the precipitated tobermorite on the surface of 908D (Fig. 8).

Gyrolite, $Ca_8Si_{12}O_{30}(OH)_4 \cdot 7H_2O$, formed on the surface of 1013D as semi-spherical groups of platelets (Fig. 6D). The structure of gyrolite is built by stacking of various structural layers: a centrosymmetric layer, S_1, characterized by six-membered rings of tetrahedra pointing alternatively upwards and downwards; an octahedral sheet, O, of edge-sharing calcium octahedra; a tetrahedral sheet, S_2, characterized by six-membered rings, presenting six downward-pointing tetrahedra to every two upward-pointing tetrahedra; and an interlayer sheet, X, consisting of calcium octahedra [25]. This sheet structure accounts for the characteristic platelet morphology of the crystals. This phase occurred frequently as a precipitate on the surface of the SRL 202U glass which was corroded for 14D at 200°C [26]. The SAED pattern (inset of Fig. 9) shows diffraction rings at 0.466, 0.346, 0.308, 0.264, 0.227, 0.183, 0.176, 0.152 and 0.133 (nm). The above SAED data are consistent with those of synthetic gyrolite (JCPDS Card 12-217). Gyrolite and apophyllite, a Ca-hydrosilicate, ideally $(K, Na)(Ca, Mg)_4(Si, Al, Fe)_8(F, OH) \cdot 9H_2O$, are major secondary minerals in hydrothermally altered basalts, sideromelane tuffs, and hyaloclastites in Iceland [27]. In addition, the paragenesis of the alteration products includes smectites (dioctahedral and trioctahedral), celadonite (a mica group member, $K(Mg, Fe^{2+})(Fe^{3+}, Al)Si_4O_{10}(OH)_2)$), zeolites, chalcedony (a fine-grained variety of quartz), opal, and calcite. The natural paragenetic association of the secondary phases are similar to these found in surface layers of the R7T7 waste glass, lending

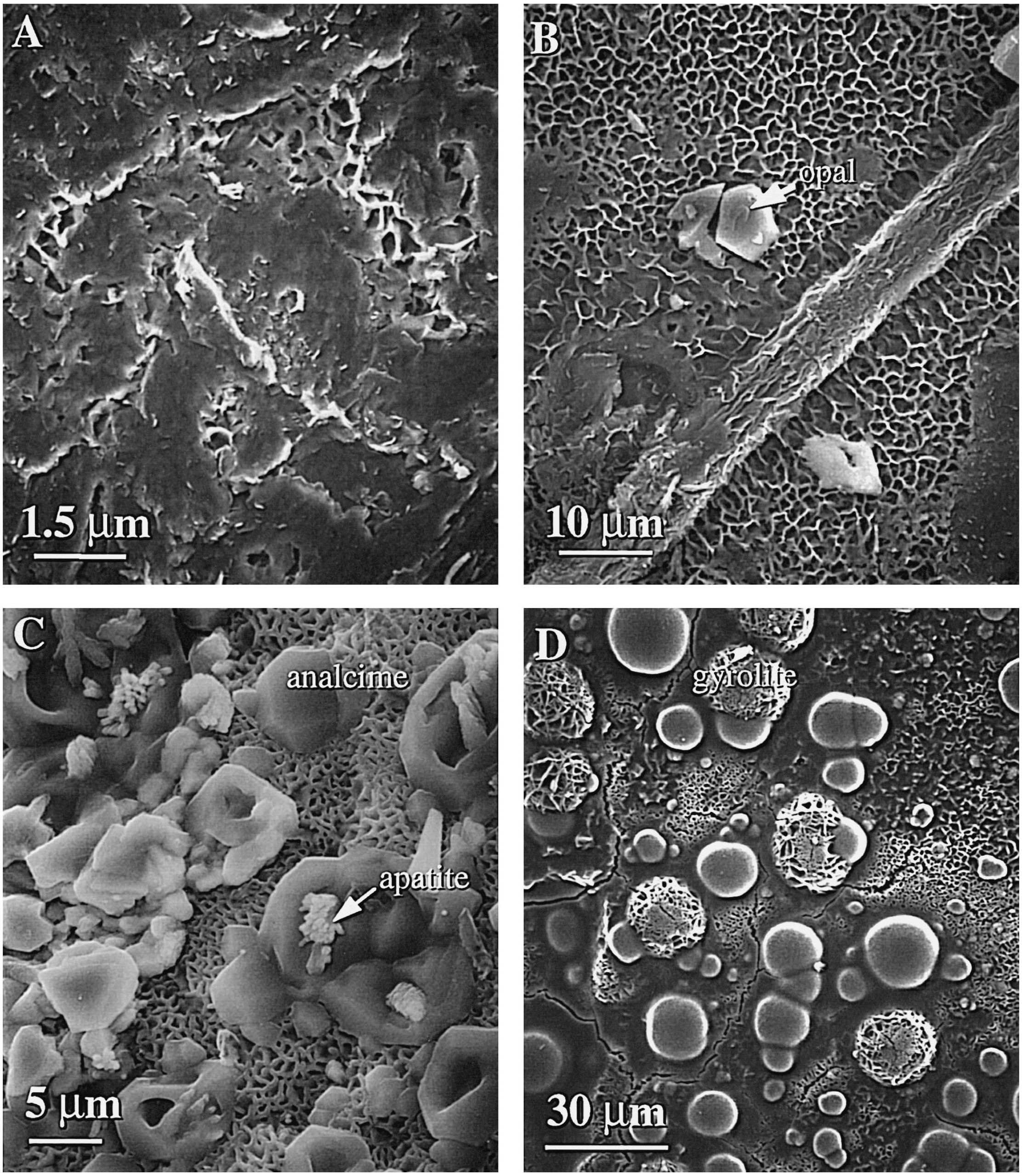

Fig. 6. A sequence of SEM micrographs showing the morphological evolution of the glass surface with increasing alteration time. (A) 91D, honeycomb-like smectite layer has only developed locally. No secondary phase was found on the surface. (B) 241D, honeycomb-like smectite layer is well developed. Only hydrated silica precipitates (opal) occur on the surface, as indicated by the arrow. (C) 908D, honeycomb-like smectite layer is well developed with precipitates on the surface. Abundant precipitates include analcime, apatite, sodium silicates (not shown), and calcium silicates (not shown). (D) 1013D, two major precipitates, gyrolite and a spherical, amorphous calcium silicate occur on the 'honeycomb' of smectite crystals. The honeycomb-like smectite layer is not as well developed as on 908D. It is possible that for the aged samples, the smectite layer was detached locally.

support to the hypothesis that the experimentally observed alteration phases can be stable over geological periods of time. In addition to gyrolite and tobermorite, other hydrated Ca-silicate phases may be present, such as afwillite, $Ca_3Si_2O_4(OH)_2$, and nekoite, $Ca_3Si_6O_{12}(OH)_6 \cdot 5H_2O$, as extensive SEM/EDS examinations of 91D, 908D, and 1021D show that Si/Ca ratios for the Ca-silicate phases range from 0.5 to 1.5. However, further identification of

Table 2
Major precipitates formed on the surface of the SON68 waste glass

	Formula	22D	91D	241D	908D	1013D	1021D	
Analcime	$Na(AlSi_2O_6)\cdot H_2O$				✓			Fig. 7
Calcium silicate	$Si/Ca = 0.5–1.5$		✓		✓	✓		Fig. 8
Apatite	$Ca_5(PO_4)_3(OH, Cl, F)$				✓		✓	Fig. 7
Weeksite	$K_2(UO_2)_2(Si_2O_5)_3\cdot 4H_2O$						✓	[23]
Sodium silicate	$Na/Si = 1–3$		✓		✓			[23]
Powellite[a]	$(Ca, Sr)MoO_4$				✓		✓	Fig. 10
Ag–Te phase[a]	Ag_2TeO_3			✓				

[a] Crystalline precipitates which grew within the inner zones of surface layers.

these Ca-silicates requires the combined use of EDS and SAED analyses. Ca-silicates such as tobermorite and gyrolite, the most frequently occurring precipitates on the surfaces of corroded waste glasses, have been found to be excellent phases for ion exchange [28]. Tobermorite with Al^{3+} substituted for Si^{4+} has an extremely high sorption selectivity for Cs, Sr, and other alkaline and alkaline-earth elements through ion exchange [29]. Thus, precipitates formed in the surface layers are potentially of importance for radionuclide retention.

Amorphous, Ca-rich silicate precipitates with a spherical morphology (10–30 μm in size) occurred on the surface of 1013D (Fig. 6D). A typical chemical composition is (wt%): SiO_2 70.91, Al_2O_3 3.51, Na_2O 2.07, CaO 12.05, FeO 2.40, ZrO_2 3.06, Ce_2O_3 0.70, and BaO 5.30. Evidently, Ba was incorporated into this precipitate in high amounts.

Additionally, two crystalline precipitates, powellite and a Ag–Te phase, were found to have formed within the inner zones of the surface layers as seen in cross-sectional AEM examinations. Fig. 10 shows that powellite occurs as small particles in less-crystallized aggregates in the surface layer. The powellite, as small particles (0.1–0.5 μm), has been positively identified by using electron microdiffraction (inset of Fig. 10). The chemical compositions of powellite samples detected in this study are listed in Table 3. A typical structural formula of powellite on a 4-oxygen basis is: $(Ca_{0.88}Sr_{0.10}Ba_{0.02})MoO_4$, which indicates that powellite is a major host for Sr. ^{90}Sr occupies the Ca site in powellite and ultimately decays to Zr^{4+}. It is likely that Zr^{4+} will substitute for Mo^{6+} in a limited amount. Because the concentration of ^{90}Sr in the powellite phase is only a few percent, the stability of the powellite structure

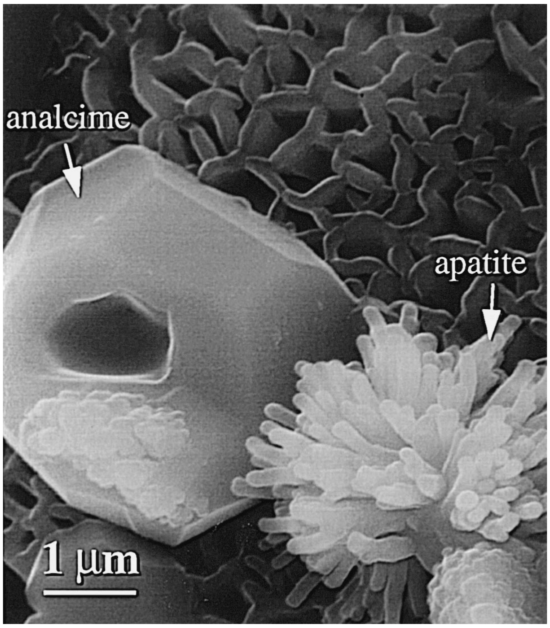

Fig. 7. SEM micrograph showing analcime and apatite precipitated on the surface of 908D. The honeycomb-like smectite layer is evident.

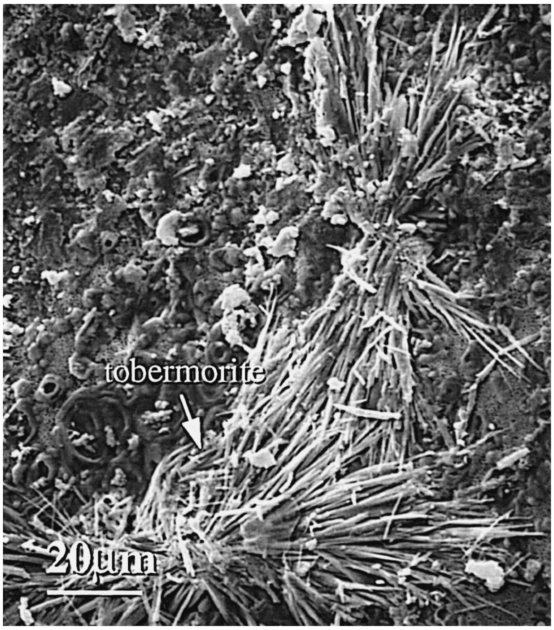

Fig. 8. SEM micrographs showing the morphology of tobermorite precipitates on the surface of 908D.

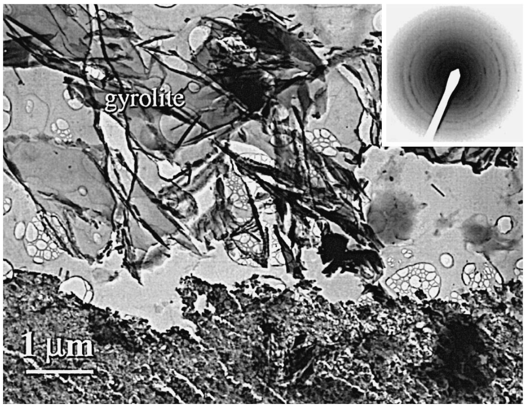

Fig. 9. BF image and SAED pattern (inset) of gyrolite on 1013D.

will probably not be affected by transmutation. The 600 keV Xe^+ irradiation study of the $Na_{0.24}RE_{0.32}Ca_{0.39}MoO_4$ crystal at room temperature indicated that the powellite was slightly more resistant to amorphization than zircon [30].

The powellite found as a precipitated phase on the surface of the R7T7 waste glass, corroded in $MgCl_2$ solution at 190°C, was particularly rich in rare-earth elements, such as Pr_2O_3 and La_2O_3 [30]. The powellite was identified on the surfaces of the French R7T7 waste glass corroded in three different halite saturated solutions: (1) high in Mg, low in Na, no Ca; (2) high in Mg and Ca, low Na; and (3) high in Na, low in Ca and Mg at temperatures up to 190°C [31]. The Mg- and Ca-rich solutions became acidic during corrosion, and the powellite characteristically had higher rare-earth element concentrations, such as in the $Na_{0.5}RE_{0.5}MoO_4$–$CaMoO_4$ solid-solution. While in the high-Na solution which finally became alkaline, pure powellite formed and rare-earth elements eventually precipitated as separate phases [31]. Whether powellite precipitates on the surface or within the inner zones of the surface layer may be determined by the initial solution composition.

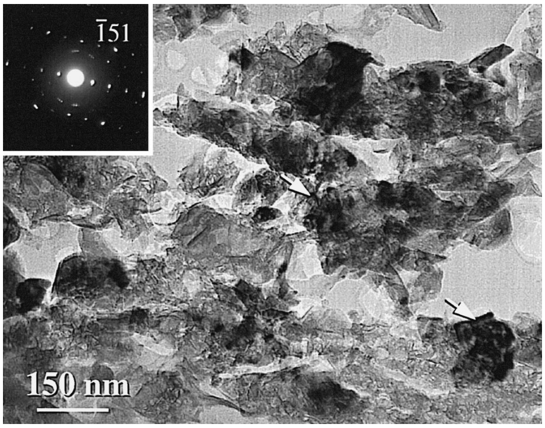

Fig. 10. BF image and SAED pattern (inset) of in situ nucleated powellites (908D, Zone 5). The arrows point to powellite.

Table 3
The chemical compositions for powellite within the surface layers

	#40	#41	#46	#47	#48	#68	#120	#169	Average
CaO	23.4	24.3	24.8	24.5	25.0	24.9	25.3	26.1	24.8
MoO_3	69.6	69.8	70.3	69.3	69.8	70.3	70.5	71.0	70.1
SrO	5.3	4.4	4.9	4.5	4.8	4.3	3.9	2.9	4.4
BaO	1.8	1.5	0.0	1.7	0.4	0.5	0.3	0.0	0.8

#40–48 are from 908D and #68–169 from 1021D.

The Ag–Te phase was only found in 241D as small particles (2–5 µm) within the surface layer. The chemical composition for this phase is rather simple, and a typical composition is: TeO_2 43.4 and Ag_2O 56.6 (wt%), conforming to a formula of Ag_2TeO_3. The occurrence of this Ag–Te phase is important, as the original abundance of Ag and Te in the SON68 glass was low (Table 1). The Ag and Te must have been transported over a long distance to form a crystalline phase in situ within the inner zones of the surface layer.

3.3. Structure of the surface layer: A- and B-domains

Zones 4 and 5 contain domains which are morphologically and chemically distinct. One consists of fibrous, coarsely crystalline, smectite aggregates, identified as A-domains. The other consists of the spherical, less-crystallized, ultrafine-grained aggregates, identified as the B-domains. The two domains are clearly seen in TEM micrographs (Figs. 11 and 12). The two domains can be easily differentiated by SAED patterns, in terms of degree of crystallinity, as shown in Fig. 13.

The smectites in the A-domains always contain relatively high concentrations of transition metal elements, such as Fe, Zn, Cr, Mn, and Ni, while Zr, Mo, and rare-earth elements are very low in concentration (Table 4). The enrichment coefficients, $E_i = C_{surf.}/C_{glass}$, for transition metal elements are >1. However, the enrichment coefficients for Zr, Mo, U, Th, and rare-earth elements are always far less than 1. The concentration of ZrO_2 is below the detect limit in the A-domains. The SiO_2 contents usually exceed the required values for the smectite stoichiometry, because EDS analyses were made on regions containing the smectite crystallites and the amorphous silica-rich matrix. Taking an A-domain as an example, the calculated formula for the mixture of smectite crystallites and the silica-rich matrix on an 11-oxygen equivalent basis is: $(Na, Ca)_{0.48}(Fe^{3+}_{0.42}Al_{0.33}Zn_{0.17}Ni_{0.16}Cr_{0.10}Mn^{2+}_{0.06})Si_{4.48}O_{10}(OH)_2$. If 55 mol% of SiO_2 accounts for the matrix silica, the smectite formula would be: $(Na, Ca)_{0.88}(Fe^{3+}_{0.77}Al_{0.30}Zn_{0.31}Ni_{0.29}Cr^{3+}_{0.19}Mn^{2+}_{0.11})(Si_{3.69}Al_{0.31})O_{10}(OH)_2$. Hence, the smectites in the A-domains are consistent with a nontronite composi-

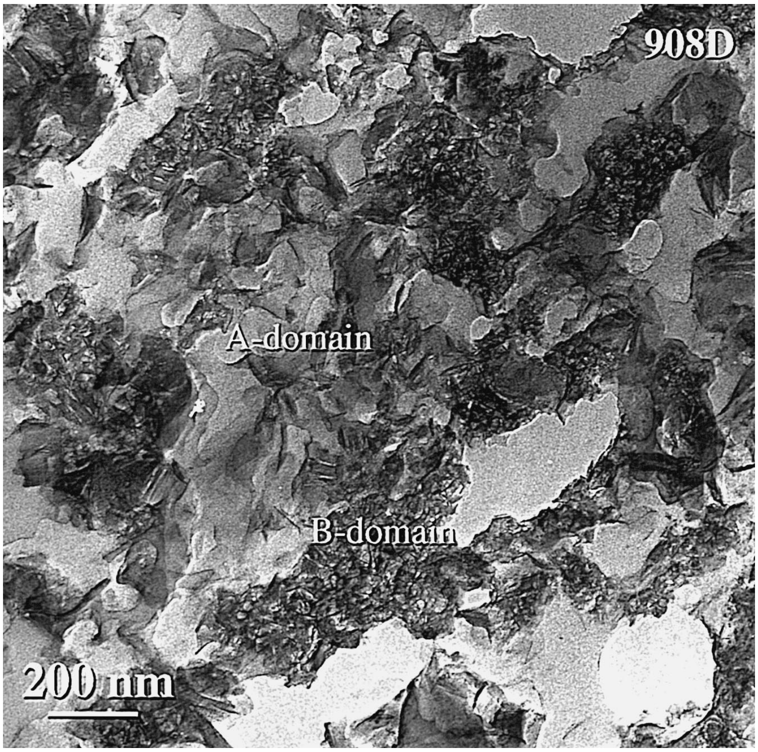

Fig. 11. TEM micrograph showing the structure of A-domains and B-domains in a surface layer (908D, Zone 5).

tion. For comparison, in a typical K-saturated nontronite, the structural formula is $K_{0.57}(Fe^{3+}_{1.84}Al_{0.15}Mg_{0.02})(Si_{3.46}Al_{0.38}Fe^{3+}_{0.16})O_{10}(OH)_2$ [32]. The SAED pattern (Fig. 13A) has diffraction rings at 0.447, 0.304, 0.257, 0.224, 0.194, 0.153, and 0.131 (nm), suggesting the 110/020, 005, 200/130, 220/040, 009, 060/330, and 400/260 spacings of a smectite structure. HRTEM imaging of these smectites shows a basal (001) spacing of 1.5 nm, as indicated by Fig. 14. Thus, the A-domain smectites are approximately identified as nontronite-1.5 nm. Since the trivalent Cr^{3+} is similar in size ($r = 0.062$ nm) and charge to Fe^{3+}, it can substitute for Fe^{3+} in dioctahedral smectites, such as nontronite and montmorillonite in which Al^{3+} is a predominant octahedral cation. The smectites containing chromium as the dominant trivalent octahedral cation are called volkonskoite. Trioctahedral smectites with Zn, Ni, and Mn as the predominant octahedral cations are refereed to as sauconite, nickel smectite, and manganese smectite, respectively. A-domain smectites are mainly members in the solid-solution series of nontronite, montmorillonite, nickel smectite, volkonskoite, and sauconite.

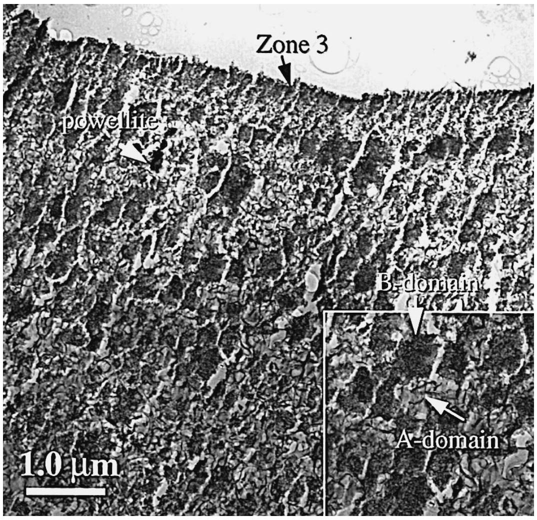

Fig. 12. TEM micrograph showing the structure of A-domains and B-domains within a surface layer (1021D).

In the B-domains, needle-like smectite crystallites occur in a somewhat spherical amorphous matrix. A typical microstructural image of the B-domains is represented by Figs. 11 and 12. The smectite crystallites (~ 10 nm in size) in the B-domains always have a basal (001) spacing of 1.8 nm. However, the SAED patterns show that B-domains are predominantly amorphous, particularly in the upper portion of the surface layer in the long-term samples (Fig. 13B). The B-domains usually have high amounts of Zr, rare-earth elements Mo and Ca. For example, ZrO_2 is extremely high (~ 12 wt%) in the B-domains of 1021D

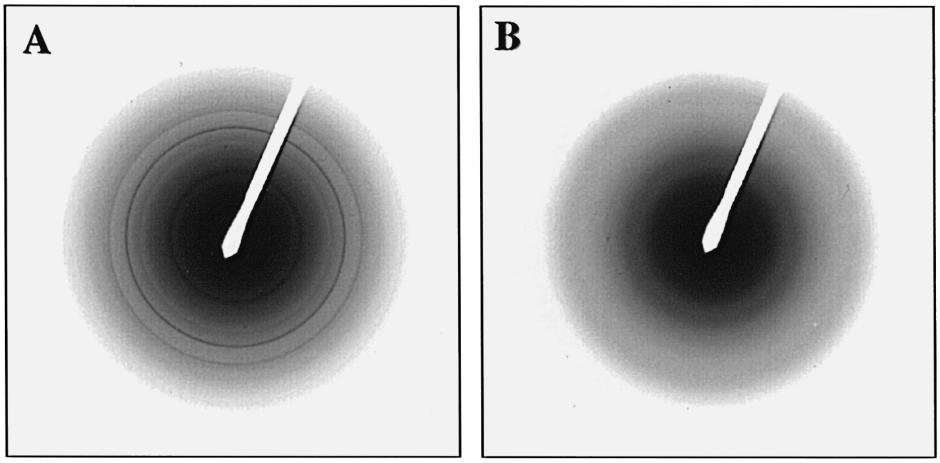

Fig. 13. Representative SAED patterns for A-domains (A) and B-domains (B) in 908D.

(Table 4). The E value (enrichment coefficient) for ZrO_2 is 4.5. The E values for rare-earth elements (e.g., La, Ce, and Nd) and Mo are all greater than 1.5, while the E values for Th and U are approximately 1. These data indicate that elements such as Zr, rare-earth elements, and Mo, may have been retained in the B-domains of the surface layers. Elements, such as the transition metal elements Fe, Zn, Cr, Mn, and Ni, as well as Na and Al, are relatively depleted in the B-domains, as compared to the A-domains and the unaltered glass (Table 4). At present, we are not able to determine the boron concentration in the surface layer. Boron may have preferentially partitioned into the B-domain, not into the A-domain, as the smectite is the dominant phase of the A-domain. In the smectite structure, there are no crystallographic sites for the boron atoms.

Table 4
Compositions of individual zones and domains of the surface layer on 1021D (wt%)

Zone N.A.	Zone 2 10	Zone 3 11	A-domain 7	B-domain 12	Zone 6[a] 8	Glass
SiO_2	63.9±3	55.3±2	69.9±3	64.4±5	64.7±3	45.48
Al_2O_3	7.8±1.5	4.6±1.5	6.2±1.0	3.7±1.0	5.6±1.0	4.91
Fe_2O_3	9.9±1.0	2.3±1.0	8.5±1.0	2.3±0.8	4.2±1.0	2.91
MnO	1.6±0.5	0.7±0.5	0.9±0.2	0.1±0.1	0.4±0.4	0.72
Cr_2O_3	0.0	0.4±0.4	1.9±0.5	0.1±0.1	0.2±0.2	0.51
Na_2O	5.7±1.0	1.5±1.5	3.1±1.0	1.5±1.5	2.2±1.0	9.86
CaO	2.1±0.5	3.4±1.0	2.6±1.0	4.8±1.5	5.0±2.0	4.04
ZnO	8.7±2.0	0.9±0.5	4.0±0.5	0.7±0.5	0.8±0.5	2.50
NiO	0.3±0.3	0.4±0.4	2.8±0.5	1.0±0.3	1.1±0.5	0.74
MoO_3	–	–	–	3.4±1.0	3.4±1.0	1.70
ZrO_2	–	11.3±2.0	–	11.9±3.0	8.8±1.5	2.65
La_2O_3	–	1.7±1.0	–	1.6±1.0	0.1±0.1	0.90
Ce_2O_3	–	10.5±2.0	–	1.8±0.5	0.6±0.6	0.93
Nd_2O_3	–	4.6±2.0	–	2.1±0.6	1.2±1.0	1.59
UO_2	–	0.3±0.3	–	0.5±0.5	1.0±0.5	0.52
ThO_2	–	2.0±1.0	–	0.6±0.6	0.2±0.2	0.33

N.A., analysis number.
[a] Including 0.44 CoO.

The A-domains in Zone 4 are more predominant in volume than the A-domains in Zone 5 in the long-term experiments (e.g., 1013D, and 1021D). The needle-like smectite crystallites were not always present in the B-domains of long-term samples. In short-term experiments (e.g., 22D, 91D, and 241D), the interface between Zones 4 and 5 is not evident. The poorly-crystallized B-domains apparently dominate the structure of the surface layer, while the well-crystallized A-domains only occur locally in the upper part of the cross-section (241D, Fig. 15). In 22D, Zones 4 and 5 are composed of the poorly-crystallized B-domains. Thus, the volume ratio of B- and A-domains in the surface layers decreases with increasing corrosion time, indicating that the alteration layer has evolved into thermodynamically more stable phases. These textures suggest an extensive recrystallization process of earlier-formed B-domains into A-domain smectites, associated with an increased cavity volume during the continued corrosion.

Near the top of Zone 4 in long-term samples such as 1013D, B-domains are very small (< 100 nm), as shown in Fig. 16A. These small B-domains are completely amorphous, and smectite crystallites cannot be detected. This must be all the remains of the larger, early-formed B-domains after the continuous recrystallization of the smectite crystallites. However, the B-domains in Zone 5 are larger in volume (Fig. 16B). The evidence provided by Fig. 16 shows the effects on the microstructure due to extensive recrystallization of earlier-formed B-domains during surface layer formation and reaction progress caused by vapor hydration.

The basic structures of surface layers have been identified as A-domains and B-domains. The chemical composi-

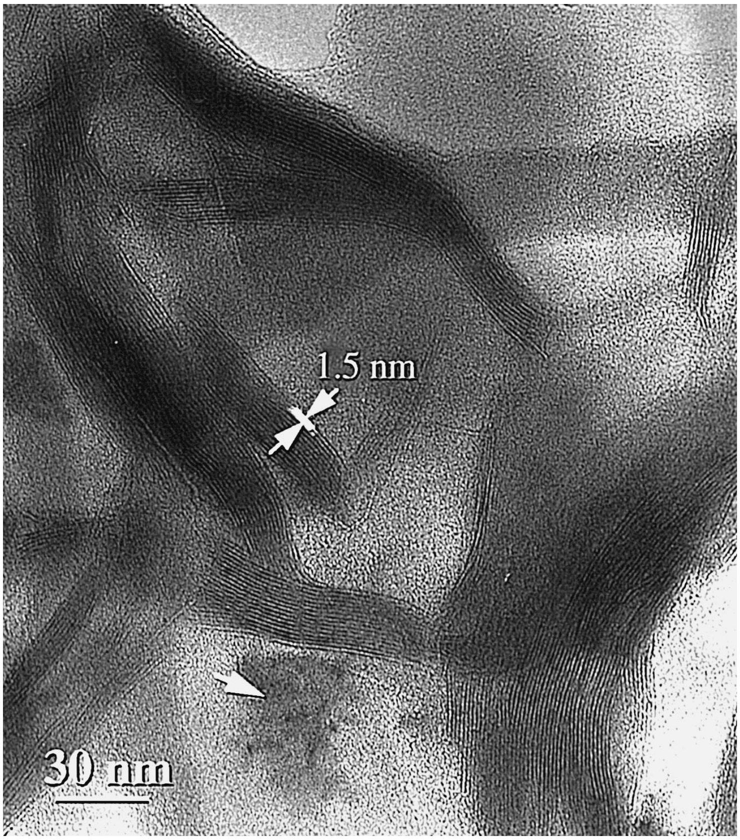

Fig. 14. HRTEM micrograph of smectites in an A-domain (1013D).

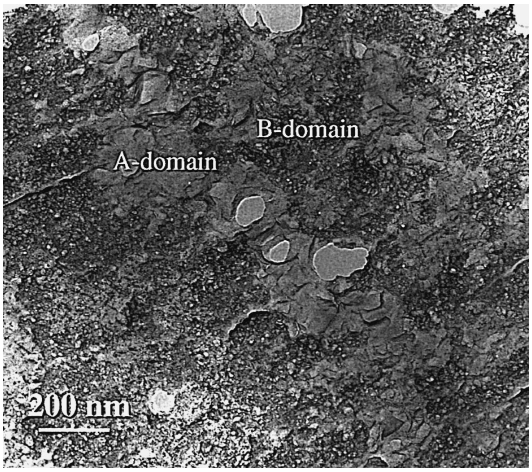

Fig. 15. TEM micrograph showing the structure of the inner zone of the surface layer in short-term samples (241D). B-domains are the dominant structures characterized by needle-like smectite crystallites in association with the spherical morphology of the amorphous matrix.

tions of the A- and B-domains are apparently different in not only sample 1012D (Table 4), but also in the other samples from 22D to 1013D, as determined by extensive EDS/AEM analyses. At an early-stage of corrosion or in the alteration front, A- and B-domains formed in-situ within the hydrated glass, as the basic structures of surface layers. All the elements are partitioned mainly between A-domains, B-domains, and possibly the pore water, since there is no bulk solution in the vapor hydration test. Transition metal elements are preferentially partitioned into A-domains; rare-earth elements, Mo and Zr, into B-domains. Na (as well as possibly Li), Zn, Ca, Al, Si, and U may be partly released into the pore solution. With continued alteration, the surface layer reorganizes in situ, and the early-formed B-domains recrystallize into A-domains. The elements redistribute again. Fig. 20 illustrates the compositional differences between individual zones and domains. Starting from an original waste glass, the nucleation zone (Zone 6) is significantly depleted in B-group oxides ($Na_2O + ZnO + MnO + Fe_2O_3 + NiO + Cr_2O_3$). During the conversion of Zone 6 to Zone 5, A-

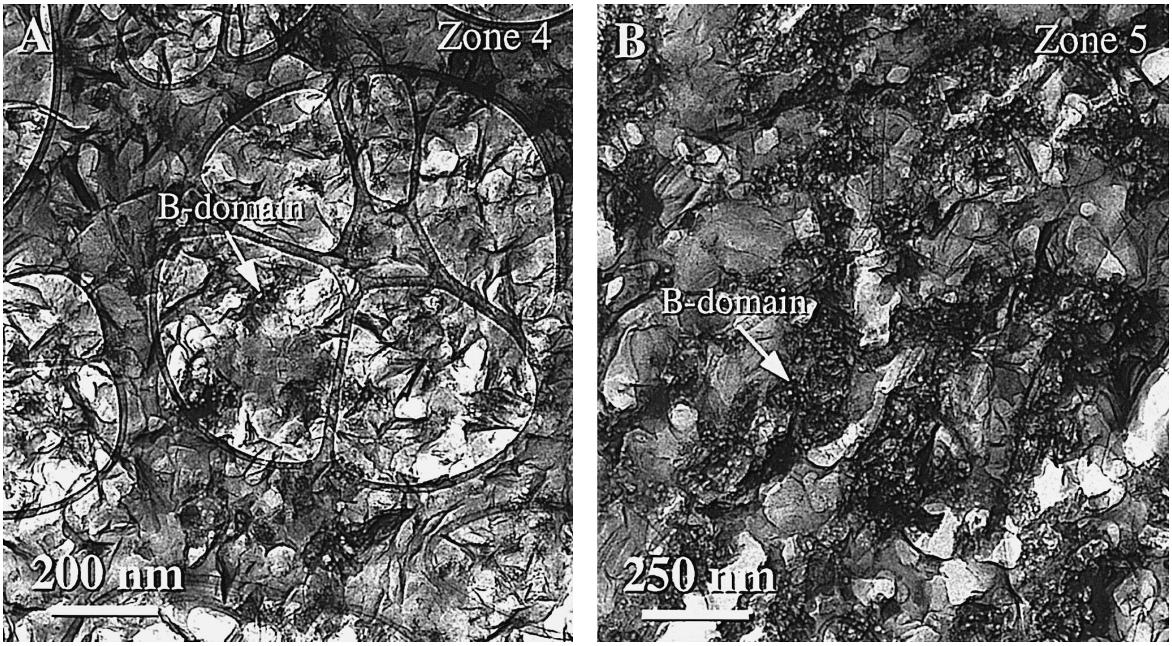

Fig. 16. TEM micrographs showing the morphological difference of B-domain structures between Zone 4 (A) and Zone 5 (B) in 908D. The Zone 5 B-domains are always larger than the Zone 4 B-domains, suggesting smectite recrystallization of earlier-formed B-domains during vapor hydration.

and B-domains inherit the overall composition of the nucleation zone, but partitioning of elements must have occurred leading to the chemical distinction between the two domains. Thus, the element partitioning among A-domains, B-domains, and possibly the pore solution, and subsequent recrystallization of the earlier-formed B-domains into the A-domain smectites are the basic processes which control the chemical evolution of the surface layer. The evolution of the chemistry and microstructure of the surface layer is very important to understanding of the long-term behavior of elements during vapor hydration.

3.4. Chemical and structural description of zones 2, 3 and 6 in surface layers

Zone 2 is present as a honeycomb-like layer occupying most of the surface, as best shown in Fig. 3B, Fig. 6C, and Fig. 7. The smectite must have grown into the solution on the original surface of the reacted glass as evidenced by the vertically oriented fibrous texture. The structural formula for smectite in Zone 2 can be calculated on an 11-oxygen basis as: $(Na_{0.72}Ca_{0.07})(Al_{0.57}Zn_{0.55}Fe^{3+}_{0.53}Mn^{2+}_{0.10}Ni_{0.01}Cr_{0.01})Si_{4.12}O_{10}(OH)_2$ (1021D). Like the A-domain smectites, the atomic fraction of Si in the formula exceeds the required value for the ideal smectite stoichiometry. If there is 20 mol% SiO_2 which accounts for silica coatings of smectite crystallites or fillings between smectite crystallites, the corrected structural formula is: $(Na_{0.86}Ca_{0.08})(Zn_{0.65}Fe^{3+}_{0.62}Al_{0.56}Mn^{2+}_{0.12}Ni_{0.02}Cr_{0.01})(Si_{3.88}Al_{0.12})O_{10}(OH)_2$. As a comparison, the structural formula of a pure sauconite clay from Zinc Village, AR, is given as: $(Ca_{0.20}Na_{0.04}$-$K_{0.4})(Zn_{1.95}Fe^{3+}_{0.58}Al_{0.17}Mg_{0.12})(Si_{3.34}Al_{0.73})_4O_{10}(OH)_2$ [33]. The Zone 2 smectites are thus mainly members in the solid-solution system of sauconite, nontronite, momtmorillonite and manganese smectite. Numerous EDS analyses of the Zone 2 smectites show that sauconite or nontronite can be dominant in short-term and long-term corroded samples. The HRTEM image of smectites in Zone 2 shows that these smectites exhibit a 1.5-nm basal spacing and that the fillings in the space between these smectite crystallites are possibly the amorphous silica which may have precipitated from the condensed water film in the cavities of the honeycomb-like smectites (Fig. 17). The SAED pattern for Zone 2 smectites (inset of Fig. 17) have electron diffraction rings at 0.452, 0.305, 0.264, 0.173, 0.153, and 0.132 (nm), suggesting the 110/020, 005, 200/130, 240/150, 060/330, and 400/260 spacings of a smectite structure which is close to sauconite-1.5 nm.

Generally, the fibrous Zone 2 smectites are similar to the A-domain smectites in composition and structure. Zr, Mo, and rare-earth elements are all relatively depleted in both the A-domains and Zone 2. However, the Zone 2 smectites are more coarsely crystalline, with a higher concentration of Zn as compared with the A-domain smectites. In A-domains, sauconite in the smectites ranges from 10 to 20%, while in the Zone 2 smectites, sauconite ranges from 25 to 40%. Unlike in the A-domains, transition metal

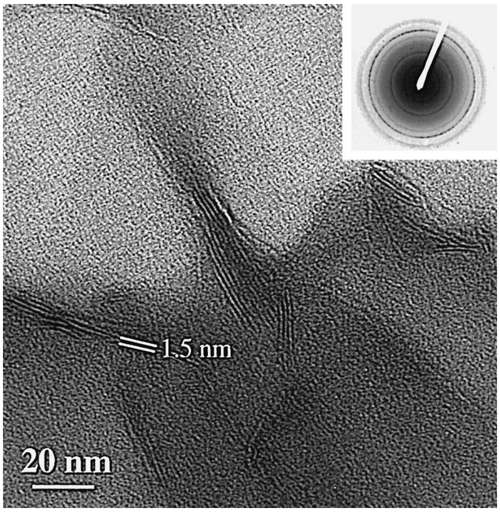

Fig. 17. HRTEM micrograph showing the microstructure of Zone 2 (241D). The inset is the corresponding SAED pattern.

elements, such as Cr and Ni, are substantially depleted as well. Assuming that Zone 2 has a precipitation origin, we infer that significant amounts of Zn, Fe, and Mn may have been partly released from the alteration layer, while Cr, Ni, Zr, Mo, Zr, and the rare-earth elements have been mainly retained within the surface layer.

Zone 2 is well developed in both the short-term corroded samples, such as 22D and 241D, and in the long-term corroded samples such as 908D. The thickness of Zone 2 increased with the duration of the vapor hydration tests: 0.2 μm for 22D, 0.4 μm for 91D, 0.6 μm for 241D, and 3 μm for 1021D (the thickness was estimated by cross-sectional TEM examinations). In addition, the vertically oriented fibrous smectite layer (Zone 2) was a common microstructure in the various waste glasses during vapor hydration [34–36].

Beneath Zone 2, there is a thin layer of an ultrafine-grained mixture of smectite crystallites and amorphous matrix (Zone 3). Structurally and chemically, Zone 3 is almost the same as the B-domains in Zones 4 and 5. However, Zone 3 has even higher concentrations of rare-earth elements and Zr than those of the B-domains (Table 4). The smectite crystallites are of one to three lattice fringe thicknesses which have a basal (001) spacing of 1.8 nm. The concentration of ZrO_2 in Zone 3 is five times higher than that of the original glass (Table 4). The ZrO_2 may be present either in the amorphous silica-rich matrix or as nm-sized particles, as revealed by a HRTEM micrograph (Fig. 18). Although the ZrO_2 concentrations both in Zone 3 and B-domains are very high (10–12 wt%), zircon ($ZrSiO_4$) crystallites were not identified. However, zircon as small particles (~ 2 μm in size) were identified within the surface layer of the SON68 waste glass corroded in $MgCl_2$ solution at 200°C for 2006 days [30].

The average concentration of rare-earth elements (the sum of La_2O_3, Ce_2O_3, and Nd_2O_3 contents) is 16.8 wt% with an E value > 5 in the Zone 3 of 1021D. Crystalline phases particularly rich in rare-earth elements were not found in this zone. Rare-earth elements may have been absorbed and immobilized within the amorphous matrix, possibly in the form of hydroxides.

Zone 6 is the smectite nucleation zone in the hydrated glassy matrix (0.5–1 μm in thickness). It is characterized by amorphous materials plus small needle-like smectite crystallites which are similar to the B-domains in structure, associated with the formation of spherical cavities (Fig. 19). The A-domain smectites are not present in this zone. The nucleation of smectite crystallites in the hydrated glass matrix is heterogeneous. Extensive EDS analyses summarized in Table 3 indicated that rare-earth elements, alkaline metals such as Na, and some of the transition metal elements such as Zn and Mn were partly removed from Zone 6 during vapor hydration, as the E values for these elements are less than 1. We presume that Li, like Na, was preferentially removed from this zone. The E values for Zr, Mo, Ni, Fe, Al, and Ca are > 1, indicating that they were not significantly removed from Zone 6. The concurrent nucleation of the smectite crystallites leads to a restructuring of the hydrated glass and the in situ redistribution of elements and is critical to its gradual conversion into Zone 5 during the formation of surface layers.

Beneath Zone 6 is the region of a homogeneous contrast, close to the nucleation zone, which should be different in structure from the fresh glass. Ion interdiffusion and

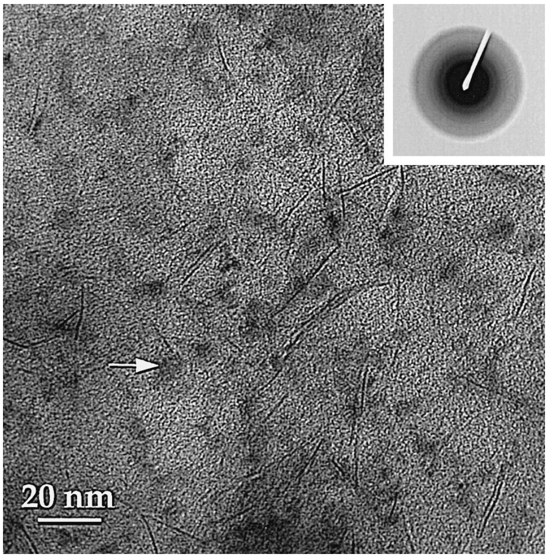

Fig. 18. HRTEM showing the microstructure of Zone 3 (1021D). Zone 3 is dominated by the amorphous phase. The needle-like crystallites are smectite. The dark spots as indicated by the arrow may be ZrO_2.

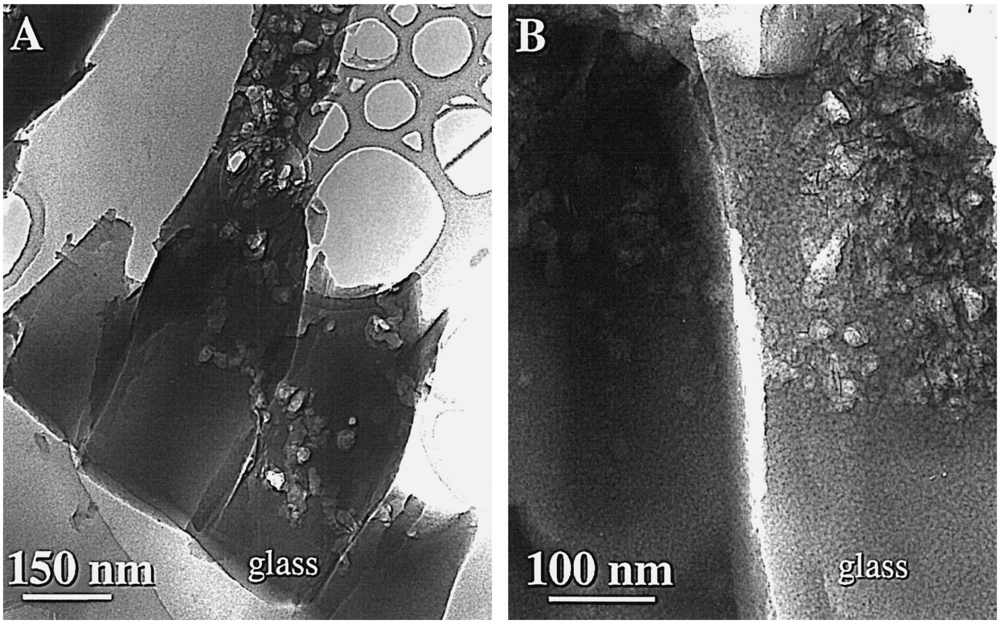

Fig. 19. TEM micrographs showing the microstructure of Zone 6. Nucleation centers of smectite are evidenced by their spherical morphology (A, 1021D) and the subsequent formation of needle-like smectite crystallites (B, 908D).

molecular water diffusion may occur during vapor hydration. Both H_3O^+ and molecular water will enter the glass structure to form a hydrated layer. The de-alkalization of hydrated layers is mainly due to the incorporation of water via molecular H_2O diffusion [8]. Thus, the glass just beneath Zone 6 is probably a hydrated and dealkalized zone. Secondary ion mass spectroscopy (SIMS) is required in order to characterize concentration profiles of alkali elements and H^+ [37].

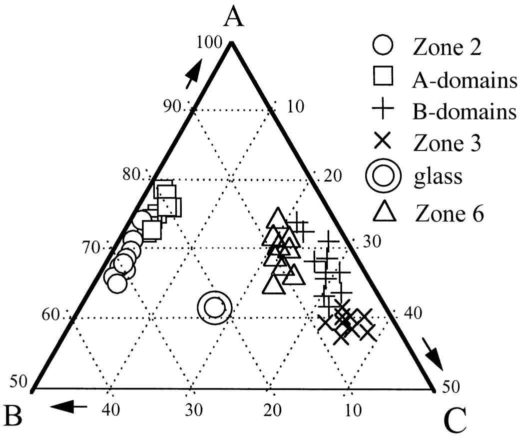

Fig. 20. Ternary plot of the major oxides in the original waste glass and individual zones and domains in the surface layers. $A = SiO_2 + Al_2O_3$, $B = Na_2O + ZnO + MnO + Fe_2O_3 + NiO + Cr_2O_3$, $C = ZrO_2 + MoO_3 + CaO + REE_2O_3$ (wt%).

3.5. Mechanism of surface layer formation

Based on the detailed observations on microstructural and compositional zoning in surface layers, the mechanism of the surface layer formation may be described as follows:

Formation of smectite nucleation zone (Zone 6). At the earliest stage of corrosion, molecular water diffuses into the random network structure of the glass and hydrolysis occurs forming the hydrated glass. The exchange of H_3O^+ from the water vapor with glass modifier elements results in continual removal of Na, Zn, Mn, and rare-earth elements from the hydrated glass. For the SON68 glass, the acidic species are more abundant than alkalis. The protonation of the non-bridging oxygen (NBO) sites due to the ion-exchange reactions catalyzes hydrolysis of adjacent borate bonds, resulting in leaching of boron and alkalis from the glass [38]. Subsequently, individual spherical centers (nm-sized), possibly nucleation sites for smectite, occur in the hydrated glass matrix. The nm-sized, needle-like crystallites of smectite grow in the amorphous matrix, forming the nucleation zone. This zone begins with hydrolysis and recondensation reactions and in situ restructuring of the hydration products, followed by partitioning and migration of elements.

Formation of Zones 4 and 5. Following smectite nucleation, the surface layer reorganizes its microstructure in situ: the smectite crystallites continue to grow into large fibrous crystals, forming well-crystallized A-domains. At the same time, the remnants of smectite crystallization in the hydrated amorphous matrix agglomerate to form individual spherical particles (B-domains). This process leads to a gradual and continual conversion of Zone 6 to Zone 5 as the hydration front proceeds steadily into the fresh glass. The progressive nucleation and growth of smectite in the previously existing B-domains results in a decrease in volume and size as seen in the upper portion of the surface layer (Zone 4), which will finally lead to a complete disappearance of the B-domains. Eventually, the majority of the surface layer volume will be very porous and well-crystallized and dominated by the presence of A-domains which are mainly composed of smectite. The geochemical behavior of the elements are principally controlled by the formation of A- and B-domains and the continued recrystallization of earlier-formed B-domains, and multiple-stage partitioning of elements among A-domains, B-domains, and the pore water during the vapor hydration process.

Formation of precipitates. As the glass corrodes, the alkalis and some other elements (e.g., alkaline-earth elements) migrate to the surface. The thin film of condensed water may become saturated with respect to phases which precipitate onto the glass surface to form a precipitation zone (Zone 1). The occurrence of analcime, calcium silicates such as gyrolite, and sodium silicates, suggests that the water film on the surface is alkaline. Because Zone 2 is present in long-term, as well as short-term, corroded samples, the Zone 2 smectites, dominated by sauconite-1.5 nm, must have precipitated on the original surface of the glass at a very early stage of the corrosion process after which they continued to grow in thickness. By incorporation of alkalis and other elements into precipitated phases, the alkali-depletion process continues. Secondary phases precipitate within inner zones as a result of restructuring of the initially formed corroded products. Formation of precipitates has been related to the observed increases in the reaction rate. The onset of the formation of specific phases results in a decrease in the concentration of elements in the water film that control the reaction affinity of the glass [39].

4. Conclusions

Surface layer zoning is evident during vapor hydration of the French SON68 waste glass at 200°C. Six zones were identified in the surface layers. The thickness of the surface layers increased slowly over the duration of experiments. The mean rate of glass alteration is $\sim 2 \times 10^{-2}$ μm per day.

A number of crystalline and amorphous precipitated phases were identified on the surface of the reacted glasses, such as analcime, gyrolite, tobermorite, apatite, sodium silicates, and weeksite. Powellite, (Ca, Sr)MoO_4 and Ag_2TeO_3 were found within the inner zones of the surface layers, indicating that Ag, Te, Sr, and Mo have been retained within the surface layers. These surface precipitates and in situ formed phases must be included in geochemical models used to predict long-term release of radionuclides during waste glass alteration and weathering.

The basic structure of a large volume of the surface layer (Zones 4 and 5) is composed of two morphologically and chemically distinct structures: The A-domains consist of fibrous, coarsely crystalline, smectite aggregates. The smectite aggregates in A-domains are composed of nontronite-1.5 nm crystallites and the amorphous silica-rich matrix. The B-domains consist of the spherical, less-crystallized, ultrafine-grained aggregates. A-domains have high concentrations of Na, Fe, and other transition metals, such as Zn, Cr, Mn, and Ni; while the B-domains have high concentrations of rare-earth elements, Mo and Zr.

During vapor hydration, the multiple-stage partitioning of elements between A-domains, and B-domains, and the pore water, and the subsequent recrystallization of the earlier-formed B-domains into the A-domain smectites are the basic processes which control the chemical and textural evolution of the surface layer. This process is very important in determining the long-term release of radionuclides under alteration of the glass.

Acknowledgements

This work was supported by the Centre D'Etudes de la Vallée du Rhône of the Commissarat à L'Energie Atomique, France. All analyses were completed in the Electron Microscopy Facility at the University of New Mexico supported by NSF, BES/DOE and the State of New Mexico. We are grateful to Ms S. Kaser for preparing some of the AEM samples. We extend special thanks to Professor W. Lutze and Dr A. Abdelouas of the University of New Mexico for their helpful discussions.

References

[1] J.L. Nogues, E. Vernaz, N. Jacquet-Francillon, Mater. Res. Soc. Symp. Proc. 44 (1985) 89.
[2] T. Murakami, T. Banba, M.J. Jercinovic, R.C. Ewing, Mater. Res. Soc. Symp. Proc. 127 (1989) 65.
[3] J.K. Bates, M.G. Seitz, M.J. Steindler, Nucl. Chem. Waste Manage. 5 (1984) 63.
[4] B. Grambow, Nuclear waste glass dissolution, model, and application, Swedish Nuclear Fuel and Waste Management Co., JSS Project Technical Report 87-02, 1987.
[5] L. Michaux, E. Mouche, J.-C. Petit, Fritz, Appl. Geochem. Suppl. (1) (1992) 21.
[6] W. Lutze, G. Malow, H. Rabe, Mater. Res. Soc. Symp. Proc. 15 (1983) 37.
[7] T.A. Abajano Jr., J.K. Bates, J.J. Mazer, J. Non-Cryst. Solids 107 (1989) 269.
[8] T.A. Abajano Jr., J.K. Bates, A.B. Woodland, J.P. Bradley, W.L. Bourcier, Clays Clay Miner. 38 (1990) 537.

[9] J.K. Bates, W.L. Ebert, X. Feng, W.L. Bourcier, J. Nucl. Mater. 190 (1992) 198.

[10] D.J. Wronkiewicz, C.R. Bradley, J.K. Bates, L.M. Wang, Mater. Res. Soc. Symp. Proc. 333 (1994) 259.

[11] Z. Andriambololona, N. Godon, E. Vernaz, Appl. Geochem. Suppl. 1 (1992) 23.

[12] W.L. Ebert, J.K. Bates, Mater. Res. Soc. Proc. Symp. 176 (1990) 339.

[13] D.J. Wronkiewicz, L.M. Wang, J.K. Bates, B.S. Tani, Mater. Res. Soc. Symp. Proc. 294 (1993) 183.

[14] E. Vernaz, J.L. Dussossoy, Appl. Geochem. Suppl. 1 (1992) 13.

[15] F. Delage, D. Ghaleb, J.L. Dussossoy, J. Nucl. Mater. 190 (1992) 191.

[16] W.L. Ebert, J.J. Mazer, Mater. Res. Soc. Symp. Proc. 333 (1994) 27.

[17] M.J. Jercinovic, S. Kaser, R.C. Ewing, Rep. to SDHA/CEA, 1991, unpublished.

[18] S. Ehret, J.L. Crovisier, J.P. Eberhart, J. Non-Cryst. Solids 86 (1986) 72.

[19] J.P. Bradley, Geochim. Coschim. Acta 52 (1988) 889.

[20] J.P. Bradley, D.E. Brownlee, Science 231 (1989) 1542.

[21] F. Delage, J. L Dussossoy, Mater. Res. Symp. Proc. 212 (1991) 41.

[22] P. Jollivet, E. Vernaz, CEA Internal Report, 1993, unpublished.

[23] W.L. Gong, R.C. Ewing, L.M. Wang, E. Vernaz, J.K. Bates, W.L. Ebert, Mater. Res. Soc. Symp. Proc. 412 (1996) 197.

[24] S.A. Hamid, Z. Kristallogr. 154 (1981) 189.

[25] S. Merlino, Miner. Mag. 52 (1988) 377.

[26] L.M. Wang, W.L. Gong, R.C. Ewing, Proc. the 31th Congress of International Geological Union, Beijing, China, 1996.

[27] A.R. Geptner, V.V. Petrova, Lithol. Polezn. Iskop. 6 (1989) 100.

[28] M. Tsuji, S. Komarneni, P. Malla, J. Am. Ceram. Soc. 74 (1991) 274.

[29] O.P. Shrivastava, S. Komarneni, Cement Concrete Res. 24 (1994) 573.

[30] A. Abdelouas, J.L. Crovisier, E. Vernaz, W. Lutze, B. Grambow, J.C. Dran, R. Müller, J. Nucl. Mater. 240 (1997) 100.

[31] A. Rother, W. Lutze, P. Schubert-Bischoff, Mater. Res. Soc. Symp. Proc. 257 (1992) 57.

[32] A.S. Besson, L.G. Dainyak, M. Rautureau, S.I. Tsipursky, C. Tchoubar, V.A. Drits, J. Appl. Crystallogr. 16 (1983) 374.

[33] C.S. Ross, Am. Miner. 31 (1946) 411.

[34] J.K. Bates, W.L. Ebert, J.J. Mazer, J.P. Bradley, C.R. Bradley, N.L. Dietz, Mater. Res. Soc. Symp. Proc. 212 (1991) 77.

[35] J.L. Crovisier, T. Advocat, J.C. Petit, B. Fritz, Mater. Res. Soc. Symp. Proc. 127 (1989) 57.

[36] A. Abdelouas, J.-L. Crovisier, W. Lutze, R. Müller, W. Bernotat, Eur. J. Miner. 7 (1995) 1101.

[37] G.G. Wicks, A.R. Lodding, M.A. Molecke, Mater. Res. Soc. Bull. 18 (9) (1993) 32.

[38] B.C. Bunker, G.W. Arnold, D.E. Day, P.J. Bray, J. Non-Cryst. Solids 87 (1986) 226.

[39] W.L. Ebert, J.K. Bates, W.L. Bourcier, Water Manage. 11 (1991) 205.